PHASE CHANGE EFFECTS ON TRANSPORT PROCESSES IN RESISTANCE SPOT WELDING

P. S. Wei [*] **T. H. Wu** [**] **S. S. Hsieh** [***]

Department of Mechanical and Electro-Mechanical Engineering
National Sun Yat-Sen University
Kaohsiung, Taiwan 80424, R.O.C.

ABSTRACT

The effects of distinct properties during phase change on mass, momentum, energy, species, and magnetic field intensity transport in workpieces and electrodes in the course of heating, melting, cooling and freezing periods in AC (alternative current) resistance spot welding are realistically and extensively investigated. Resistance spot welding has been widely used in joining thin workpieces due to its light weight and easy manufacturing. This study accounts for electromagnetic force, heat generations at the electrode-workpiece interface and faying surface between workpieces, and dynamic electrical resistance taking the sum of temperature-dependent bulk resistance of the workpieces and contact resistances at the faying surface and electrode-workpiece interface. The contact resistance is a function of hardness, temperature, electrode force, and surface condition. Instead of dealing with specific materials, this work is a general dimensionless investigation of resistance spot welding of materials with different specific heat and thermal conductivity ratios subject to realistic working parameters. The computed results show that nugget formation is delayed and heat transfer is reduced by increasing solid-to-liquid thermal conductivity and liquid-to-solid specific heat ratio. The corresponding thermal fields and flow patterns are also presented.

Keywords : Resistance spot welding, Thermal properties, Nugget formation, Phase change.

1. INTRODUCTION

Resistance spot welding has been widely used in joining thin workpieces due to its light weight, easy manufacturing and mass production. The materials to be welded are brought together under pressure by a pair of electrodes, and a heavy current is passed through them. This set up local heat because of the electrical resistance of the faying surface, causing the materials to become molten, and join together. The molten nugget grows until current flow is terminated. The nugget solidifies due to cooling through electrodes.

Heating a metal during welding affects its structure, determined by temperature, the time the metal is maintained at that temperature, cooling rate, and the composition of the metal [1-3]. The extent of the heat-affected zone depends largely on the energy input and welding time. Short time for welding of any material obviously reduces the extent of the heat-affected zone. However, with low-alloy steels and other heat-treatable alloys, although the short welding time restricts the heat-affected zone, it will increase the rate of cooling, and enhance the hardening of the weld, tendency to form shrinkage cracks and porosity. Weld hardness can increase rapidly with small increase in carbon content in steels, while porosity also increases with overheating. Relative long welding times, on the other hand, will reduce the rate of cooling and, in some instances, the weld hardness, but my give rise to excessive indentation of the electrodes. Expulsion thus more susceptibly occurs for high welding current and time than applied electrode force in high-strength cold-rolled sheet steels [4].

The grain structure after solidification in welding reflects cooling conditions. The direction of the columnar grains is always along the direction of heat flow during cooling. Since the cooling rate is the highest in the direction of electrode, it is common that the directions of columnar grains growing in these samples are roughly perpendicular to the welded sheet metal [5]. Similar microsturctures affected by thermal field in micro-resistance spot welding were presented by Zhou *et al*. [6], Ely and Zhou [7], and Xu and Zhai [8]. Gould and Chang [9] observed that in resistance spot welding of low carbon steels the solidification structure ranged from cellular at the fusion zone, heat affected zone boundary, to cellular dendritic at the faying surface. Furthermore, the finest cell/dendrite spacing was near the fusion zone-heat affected zone interface, and the coarsest spacings were at the weld centerline. Based on a one-dimensional thermal model accounting for melting, temperature dependent material properties,

[*] Professor, corresponding author [**] Graduate student [***] Professor

DOI : 10.1017/jmech.2011.3
Copyright © 2011 The Society of Theoretical and Applied Mechanics, R.O.C.
https://doi.org/10.1017/jmech.2011.3 Published online by Cambridge University Press

effective heat transfer in the liquid, electrode geometry and contact resistance, and measured temperature, primary dendrite spacing can be predicted. However, the generated isothermal transformation diagrams could not predict the martensitic microsturctures due to the inability to make accurate temperature measurements at the required speeds. Wang *et al*. [10] summarized that the nugget microstructure of most metals (*i.e.* steel, Mo, Ni, Ti alloy and Cu alloy) is a columnar dendritic structure and that of a few metals (*i.e.* Al alloy) is columnar grains around periphery and equiaxed grains in the centre. The nugget of Mg alloy only consists of an equiaxed dendritic structure in the absence of columnar dendritic grains, which are different from other materials. A more detailed investigation of thermal field is therefore required.

Some pores were observed to occur on the edges of weld nugget, and large pores were in the center of weld zone in refractory alloy 50Mo–50Re (w_t %) sheets, as presented by Xu *et al*. [5]. The weld joints in alloys produced by powder metallurgy often contain voids produced by residual volatile materials. Aside from nucleation and growth of the bubble entrapped by solidification front [11], the large pores in the center of nugget might be also produced by metal expulsion upon welding [5]. Further work needs to be done to understand the mechanism for the formation of these large pores in the nugget.

Measurements of the temperature distribution and the cooling rates are difficult for resistance spot welding due to its short time welding and invisible liquid nugget. Numerical simulation therefore is an effective tool for understanding resistance spot welding process in quantitative details. Wei and Yeh [12] was the first to propose an unsteady, axisymmetric model to investigate the effects of the physical, thermal, and metallurgical properties and welding conditions on nugget growths with mushy-zone phase change during resistance spot welding. The electromagnetic force, joule heat and interfacial heat generation, and cooling effects of electrodes are taken into account. Fluid patterns, temperature fields, and solute distributions in the liquid, solid, and mushy zones are determined. It was found variations of properties strongly affect the nugget growth. In view of parallel electric current, small Lorentz force induced small velocity around 5mm/s, contradicting experimental observation from Cunningham and Begeman [13]. Furthermore, the contact resistance is idealized by a linear decreasing function of temperature, as proposed by Gould [14], and used by Wei and Ho [15].

Feng *et al*. [16] proposed an axisymmetric finite element model for predicting distribution of temperature and nugget growth in resistance spot welding of AZ31B Mg alloy. It showed that thermal properties for different alloys play important roles in different nugget growth behavior. The onset time for nugget formation of Mg and Al alloys was about the same, which was less that that of mild steel. The more rapid increase in temperature of Mg and Al alloys than that of the mild steel was intuitionally attributed to different specific heats. Thermal conductivity of magnesium alloy was smaller than that of aluminum alloy and greater than that of mild steel in solid phase. The rate of heat loss of magnesium alloy from the weld region thus was smaller than that of aluminum alloy and greater than that of mild steel. The welding current lever required for magnesium alloy was slightly lower than that for aluminum alloy, but higher than that for low carbon steel. In fact, understanding of nugget growths in different materials cannot simply attributed to single thermal property in single phase.

Simulations of resistance spot welding should account for not only materials properties, but also realistic AC current, dynamic resistance, thermal convection, and magneto-hydrodynamics. Welding current in resistance spot welding is AC. A major defect for DC spot welding is expulsion, which is a consequence of incessant heat generation and high temperature and liquid pressure [17]. The dynamic resistance takes the sum of the bulk resistance of the two workpieces, and contact resistances at the faying surface and two electrode-workpiece interfaces. It should reflect an initial drop due to the rupture of the surface film, an increase after the breakdown of contact resistance due to the heating of the workpiece, and the subsequent fall after the maximum resistance has been reached due to the growth of the nugget diameter or the increasing penetration of the electrodes into the workpiece [18]. Since electric currents spread strongly on entering the workpiece [19], the induced electromagnetic force gives rise to strong convection in the molten nugget [20,21].

This study is to apply previous work [12,20,22] to extensively, generally, and realistically study transport processes during resistance spot welding experiencing heating, melting, cooling and freezing periods by accounting for distinct properties from solid-liquid phase transition. The nugget shape after solidification and cooling rate during freezing period, which are essentially required for analyzing microstructures of weld nugget in metallurgical and materials fields, are also presented.

2. SYSTEM MODEL AND ANALYSIS

Resistance spot welding, as illustrated in Fig. 1, is in a cylindrical coordinate system with the origin at the intersection of the axisymmetric axis and bottom electrode-workpiece surface. Workpieces are a binary alloy of radius r_b and total thickness L. The electrode has a truncated cone face with radius r_e, outer radius r_o and outer radius of the coolant hole r_c. AC is imposed on the top of the electrode. The major assumptions made are the same as previous work [12,20,22], and they are that (1) heat generations at the faying surface and electrode-workpiece interface are considered as volumetric heat sources, (2) the mushy zone is a porous medium, (3) mean values of properties within the temperature range considered are chosen and allowed to be distinct between phases.

https://doi.org/10.1017/jmech.2011.3 Published online by Cambridge University Press

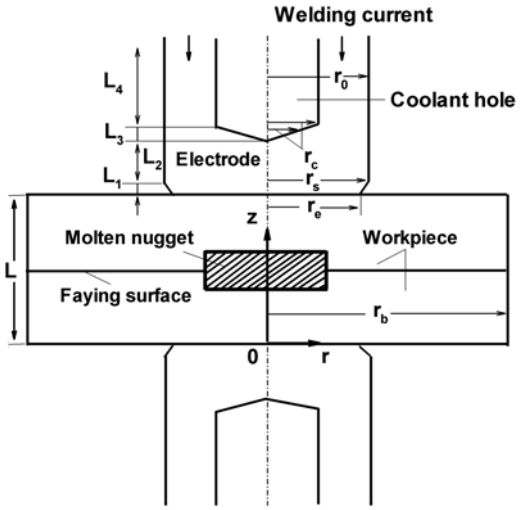


Fig. 1 Sketch for resistance spot welding and coordinate system

2.1 Governing Equations and Boundary Conditions

With the above assumptions, the dimensionless continuity, momentum, energy, species, magnetic field intensity equations [20,22], respectively, become

$$\frac{\partial \rho}{\partial \tau}+\nabla\cdot(\rho\mathbf{V_m})=0 \tag{1}$$

$$\begin{aligned}\frac{\partial \rho u_m}{\partial \tau}+\nabla\cdot(\rho\mathbf{V_m}\,u_m)&=\mathrm{Pr}\,\nabla\cdot(\rho\nabla u_m)\\&-\frac{\mathrm{Pr}}{Da}\frac{\rho(1-g_\ell)^2}{g_\ell^3}u_m-\frac{\partial p}{\partial z}\\&+\mathrm{Pr}^2 Gr\left[\theta_0(T-T_{\mathrm{sol}})+F_0(f_\ell^{\alpha}-f_{\ell,\mathrm{Tsol}}^{\alpha})\right]\\&-\frac{Lo}{\pi^2}\mu_r\,H\frac{\partial H}{\partial z}\end{aligned} \tag{2}$$

$$\begin{aligned}\frac{\partial \rho v_m}{\partial \tau}+\nabla\cdot(\rho\mathbf{V_m}\,v_m)&=\mathrm{Pr}\,\nabla\cdot(\rho\nabla v_m)\\&-\frac{\mathrm{Pr}}{Da}\frac{\rho(1-g_\ell)^2}{g_\ell^3}v_m-\frac{\partial p}{\partial r}\\&-\frac{Lo}{\pi^2}\frac{\mu_r}{r}H\frac{\partial rH}{\partial r}\end{aligned} \tag{3}$$

$$\begin{aligned}\frac{\partial \rho h_m}{\partial \tau}+\nabla\cdot(\rho\mathbf{V_m}\,h_m)&=C\nabla\cdot(K\nabla h_m)\\&+C\nabla\cdot\left[K\nabla(h_s-h_m)\right]-\nabla\cdot\left[\rho(h_\ell-h_m)\mathbf{V_m}\right]\\&+\frac{Lo\,\Sigma}{\pi^2}\left(\frac{1}{\sigma_c}+\frac{1}{\sigma}\right)\left[\left(\frac{1}{r}\frac{\partial rH}{\partial r}\right)^2+\left(\frac{\partial H}{\partial z}\right)^2\right]\end{aligned} \tag{4}$$

$$\begin{aligned}\frac{\partial \rho f_m^{\alpha}}{\partial \tau}+\nabla\cdot(\rho\mathbf{V_m}\,f_m^{\alpha})&=\frac{\mathrm{Pr}}{Sc}\nabla\cdot(\rho f_\ell\,\nabla f_m^{\alpha})\\&+\frac{\mathrm{Pr}}{Sc}\nabla\cdot\left[\rho f_\ell\nabla(f_\ell^{\alpha}-f_m^{\alpha})\right]\\&-\nabla\cdot\left[\rho(f_\ell^{\alpha}-f_m^{\alpha})\mathbf{V_m}\right]\end{aligned} \tag{5}$$

$$\begin{aligned}\frac{\partial \mu_r H}{\partial \tau}+\nabla\cdot(\mu_r H\mathbf{V_m})&=\mathrm{Pr}_m\,\nabla\cdot\left(\frac{1}{\sigma}\nabla H\right)\\&+\mathrm{Pr}_m\left[\frac{H}{r}\frac{\partial}{\partial r}\left(\frac{1}{\sigma}\right)-\frac{H}{\sigma r^2}\right]+\frac{\mu_r H\mathrm{v_m}}{r}\end{aligned} \tag{6}$$

where all lengths are nondimensionalized by the outer radius of the electrode, whereas time is nondimensionalized by the time for thermal diffusion $\tilde{r}_o^2/\tilde{\alpha}_\ell$. Dimensionless parameters are, respectively, defined as

$$\begin{aligned}&\mathrm{Pr}\equiv\frac{\tilde{\nu}_\ell}{\tilde{\alpha}_\ell},\quad \mathrm{Pr}_m\equiv\frac{\tilde{\eta}_\ell}{\tilde{\alpha}_\ell},\quad \mathrm{Da}\equiv\frac{\mathrm{K_o}}{\tilde{r}_o^2},\\&\mathrm{Gr}\equiv\frac{g\beta_T(\tilde{T}_{\mathrm{sol}}-\tilde{T}_{\mathrm{e}})\,\tilde{r}_{\mathrm{o}}^3}{\tilde{\nu}_\ell^2},\quad \theta_0\equiv\frac{\tilde{T}_0}{\tilde{T}_{\mathrm{sol}}-\tilde{T}_{\mathrm{e}}},\\&Fo\equiv\frac{\beta_s\,\tilde{f}_{m,0}^{\alpha}}{\beta_T(\tilde{T}_{\mathrm{sol}}-\tilde{T}_{\mathrm{e}})},\quad \mathrm{Lo}\equiv\frac{I^2\mu_0\,\mu_{r\ell}}{\tilde{\rho}_\ell\,\tilde{\alpha}_\ell^2},\\&C\equiv\frac{\tilde{c}_\ell}{\tilde{c}_s},\ \Sigma\equiv\frac{\tilde{\rho}_\ell\,\tilde{\eta}_\ell}{\tilde{r}_o^2\,h_f},\quad \mathrm{Sc}\equiv\frac{\tilde{\nu}_\ell}{\tilde{D}_\ell^{\alpha}}\end{aligned} \tag{7}$$

The last terms on the right-hand side of Eqs. (2) and (3) stand for Lorentz force. The last term on the right-hand side of Eq. (4) combines heat generation at contact surfaces and in bulk workpieces. Determinations of distinct regions of the mushy zone, full liquid and solid have been presented in details by Bennon and Incropera [23] and Wei and Yeh [12]. In view of irregular phase domain of electrodes, an immobilization transformation can be effectively used. Energy and magnetic field intensity equations in the electrodes thus, respectively, become

$$\begin{aligned}\frac{\partial T_E}{\partial \tau}&=\frac{k_E\,k_s\,RC}{\rho_E\,R_E}\left[\frac{\partial^2 T_E}{\partial\zeta^2}+\left(\frac{1}{N^2}+M^2\right)\frac{\partial^2 T_E}{\partial\xi^2}+2M\frac{\partial^2 T_E}{\partial\xi\,\partial\zeta}\right.\\&\left.+\left(\frac{1}{\xi N+r_c}-2M\frac{dN}{d\zeta}\right)\frac{1}{N}\frac{\partial T_E}{\partial\xi}\right]\\&+\frac{Lo\,\Sigma}{\pi^2\rho_E\,R_E\,\sigma_E}\left[\left(M\frac{\partial H_E}{\partial\xi}+\frac{\partial H_E}{\partial\zeta}\right)^2\right.\\&\left.+\left(\frac{H_E}{\xi N+r_c}+\frac{1}{N}\frac{\partial H_E}{\partial\xi}\right)^2\right]\end{aligned} \tag{8}$$

$$\begin{aligned}\frac{\partial H_E}{\partial \tau}&=\mathrm{Pr}_m\,\eta_E\left[\frac{\partial^2 H_E}{\partial\zeta^2}+\left(\frac{1}{N^2}+M^2\right)\frac{\partial^2 H_E}{\partial\xi^2}+2M\frac{\partial^2 H_E}{\partial\xi\,\partial\zeta}\right.\\&\left.+\left(\frac{1}{\xi N+r_c}-2M\frac{dN}{d\zeta}\right)\frac{1}{N}\frac{\partial H_E}{\partial\xi}-\frac{H_E}{(\xi N+r_c)^2}\right]\end{aligned} \tag{9}$$

Boundary conditions associated with Eq. (9) for magnetic field intensity at the top of the upper electrode

$$H_E=-\frac{1}{2(1+r_c)}\frac{\xi^2(1-r_c)+2r_c\,\xi}{\xi(1-r_c)+r_c}\sin 2\pi\omega\tau \tag{10}$$

which is obtained by assuming uniform current across the top surface. Magnetic field intensity vanishes in the coolant hole because of negligible electric current.

https://doi.org/10.1017/jmech.2011.3 Published online by Cambridge University Press

Magnetic field intensity at the electrode-workpiece interface is satisfied by continuities of tangential electric and magnetic field intensities across the interface, respectively. Magnetic field intensity must vanish at the axisymmetric axis to avoid infinite electric currents.

2.2 Electrical Contact Resistance

A local dimensionless electrical contact resistance at the faying surface or electrode-workpiece interface can be simulated by [22]

$$R_c = \frac{R_1}{\sigma}\sqrt{nH_v} + R_2\frac{snH_v}{\sigma_f} \tag{11}$$

where dimensionless parameters governing constriction and film resistances are, respectively, defined as

$$R_1 \equiv \frac{1}{2\tilde{R}_0\,\tilde{\sigma}_{liq}}\sqrt{\frac{\pi\tilde{H}_{v0}}{W}}\,, \quad R_2 \equiv \frac{r_o\,\tilde{H}_{v0}}{W\tilde{R}_0\,\tilde{\sigma}_{liq}} \tag{12}$$

Since electrical properties and hardness depend on temperature, electrical contact resistance governed by Eqs. (11) and (12) involves transient coupling between thermal-mechanical effects. Each of conservation Eqs. (1)-(6), (8) and (9) is discretized by the control-volume, implicit finite-difference scheme with staggered grids [24]. A grid system 50 × 53 in workpieces and 27 × 72 in the electrode were selected. The axial direction is divided into uniform spaces while the spacing ratio in the radial direction is 0.95. A dimensionless uniform time step was 2×10^{-5}. The maximum deviation of the computed resistances by using grid systems of 50 × 53 and 72 × 75 is less than 1%. The convergence tolerances for global energy and velocity components and enthalpy, concentration, and magnetic intensity fields were 10^{-2} and 10^{-3}, respectively. Otherwise, equations for the electrode were solved again and the process was repeated. If solutions converged, temperature distributions were used to calculate resistances. Computations then proceeded to the next time.

3. RESULTS AND DISCUSSION

In this study, the characteristics of distinct thermal properties experiencing phase transition on transport processes during heating, melting, cooling and freezing periods are realistically determined. The present work uses the computer program with a successful model for dynamic electric resistance [22] to determine unsteady mass, momentum, energy, species and magnetic field intensity transport in workpieces and electrodes. Dynamic electrical resistance takes the sum of temperature-dependent bulk resistance of workpieces and contact resistances at the faying surface and electrode-workpiece interfaces. The contact resistance is composed of constriction and film resistances, which increase with decreasing electrode force and increasing hardness and number of contact spots at interfaces. Hardness also decreases with increasing temperature. Sizes of contact spots on contact surfaces can also be a function of the electrode force, total number of contact spots, and hardness. Interactions between these factors should reveal the facts that an increase in temperature decreases film resistance, while increases constriction resistance and bulk resistance in workpieces. Dimensionless parameters governing constriction and film resistances at the faying surface are $R_1 = 30$ and $R_2 = 30$, which were estimated by choosing typical values $\tilde{\omega} = 60\text{Hz}$, $\tilde{R}_0 = 10^{-4}\,\text{ohm}$, $\tilde{H}_{v0} = 10^8\,\text{N/m}^2$, $W = 1000\,\text{N}$, $\tilde{\sigma}_{liq} = 10^6\,\text{mho/m}$, and $\tilde{r}_o = 10^{-2}\,\text{m}$.

This model is confirmed from a good agreement with a measured relationship between nugget thickness provided by Gould [14] in welding AISI 1008, as shown in Fig. 2. In this case, solute concentration $\hat{f}^{\alpha}_{m,0} = 0.32$ w_t % of Mn in a Fe-Mn alloy, total thickness of the two workpieces $L = 0.715$, electrode tip radius $r_e = 0.9$, dimensionless parameter governing Lorentz force (or welding current) $L_o = 6.17 \times 10^8$, and constriction and film resistance parameters $R_1 = 100$ and $R_2 = 50$. This work shows a better agreement with the experimental result than the one-dimensional prediction from Gould [14]. The former neglected heat transfer in the radial direction so that thicknesses of the nugget are overestimated.

The isothermals in the workpieces and electrode at dimensionless times of 0.543 and 0.590 are shown on the right- and left-hand parts in Fig. 3(a), respectively. Dimensionless parameters are chosen to be dimensionless total thickness of workpieces $L = 0.8$, parameter governing Lorentz force $L_o = 4 \times 10^7$, and current frequency $\tilde{\omega} = 60\text{Hz}$. The times chosen are, respectively, at the instants when thicknesses of the liquidus line are 0.4L during heating and melting period, and zero during cooling and solidification period. It can

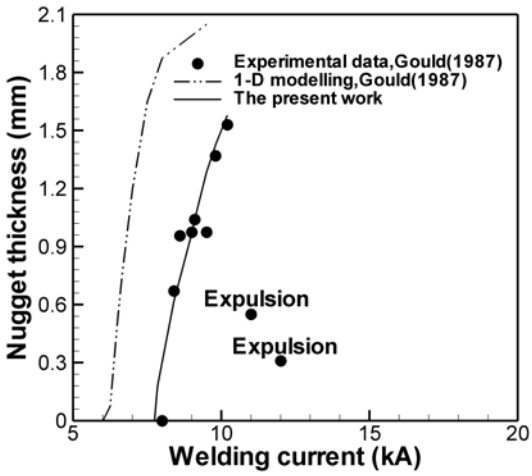


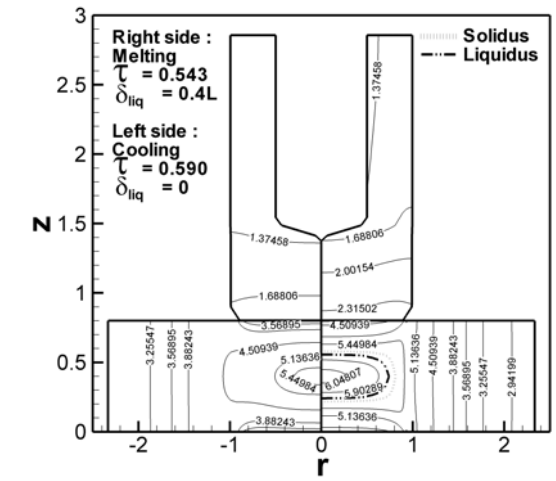
Fig. 2 Comparisons of nugget thickness versus welding current in welding AISI 1008 steel between one-dimensional predications and measurements from Gould [14] and this work

https://doi.org/10.1017/jmech.2011.3 Published online by Cambridge University Press

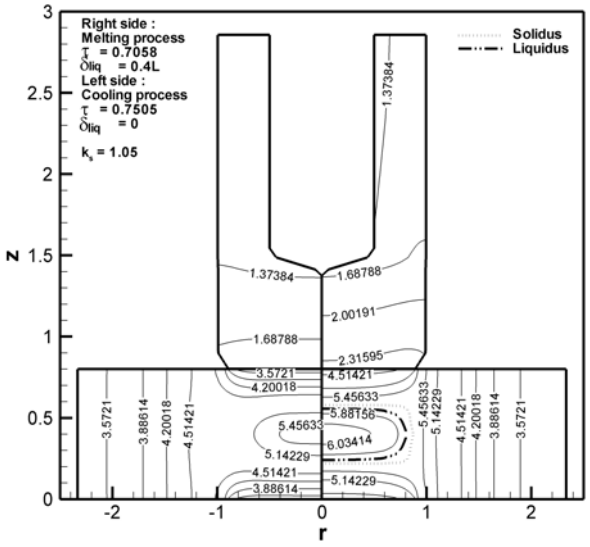
be seen that the highest temperature around 6.2 roughly corresponding to 1800K takes place near the center of the workpieces during the melting process. The spatial variation of temperatures in workpieces and electrode during cooling period is less than that during melting period. As the solid-to-liquid thermal conductivity ratio increases to 1.05 from unity, the isothermals at two times when nugget thicknesses are 0.4L and zero are shown in Fig. 3(b), respectively. In comparison to previous Fig. 3(a), which needs a dimensionless time of 0.543 to reach nugget thickness of 0.4L, the molten nugget delineated by the dotted line representing the solidus line expands slowly. This is because it needs a longer dimensionless time of 0.706 to reach nugget thickness of 0.4L. Energy balance at the melting front (namely, the Stefan boundary condition) indicates that thermal conduction from the liquid to the interface must be balanced by thermal conduction dissipated to the solid and absorption of latent heat from transition of solid to liquid. Melting rate therefore reduces with increasing solid-to-liquid thermal conductivity ratio due to a decrease in latent heat absorption. On the other hand, complete solidification needs less time or solidification rate increases because time span for complete solidification is 0.045 in comparison with 0.047 (see Fig. 3(a)) This is attributed to enhanced heat conduction to the solid and electrodes from an increase in solid thermal conductivity. As liquid-to-solid specific heat ratio decreases, melting rate increases, as can be seen in Fig. 3(c). Specific heat represents energy required to raise a unit temperature for a given unit mass. A decrease in liquid-to-solid specific heat ratio therefore produces a higher liquid temperature and a lower solid temperature. Heat conduction from the liquid to solid thus is enhanced. On the other hand, in the course of solidification, the freezing rate decreases with liquid-to-solid specific heat ratio. This is attributed to a decrease in energy loss to the solid due to a decreased temperature difference between liquid and solid.

The flow patterns at the time when nugget thickness is 0.4L are shown in Fig. 4(a). In view of divergent electric current, Lorentz force induces the vertex cell circulating in counterclockwise direction away from the axisymmetric axis in the upper workpiece. The dimensionless maximum speed is 10.8, which approximately corresponds to 0.1 m/s for typical steels. The shape of the cell looks like an ellipse. Similar flow patters in the case of an increase in solid-to-liquid thermal conductivity ratio can be seen in Fig. 4(b). As liquid-to-solid specific heat ratio decreases, the other small vortex cell in clockwise direction is found near the axisymmetric axis in Fig. 4(c). The original, outer cell is displaced toward the axisymmetric axis.

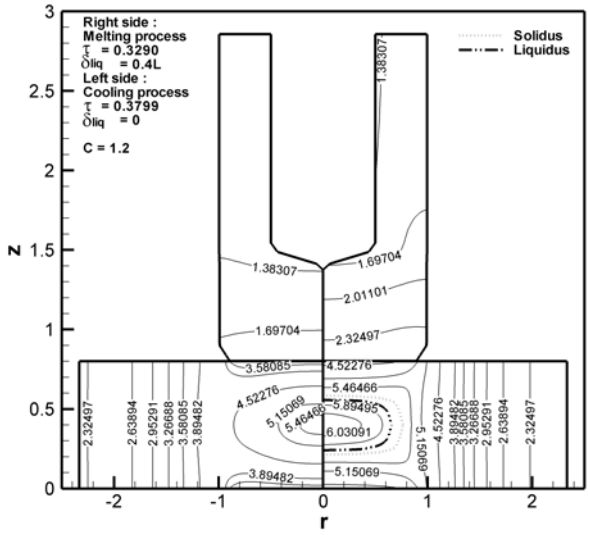
The corresponding heat transfer rates in radial and axial directions affected by solid-to-liquid thermal conductivity ratio and liquid-to-solid specific heat ratio are shown in Figs. 5(a) and 5(b), respectively. Heat transfer rate in the axial direction is roughly two times higher than that in the radial direction. As a consequence, columnar microstructure can be seen in resistance spot welding, as mentioned previously. This is the reason why conventional one-dimensional thermal



(a) $k_s = 1$, $C = 1.4$



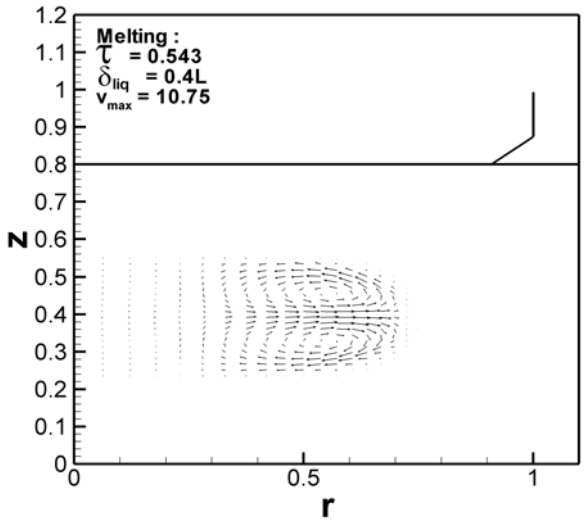
(b) $k_s = 1.05$, $C = 1.4$



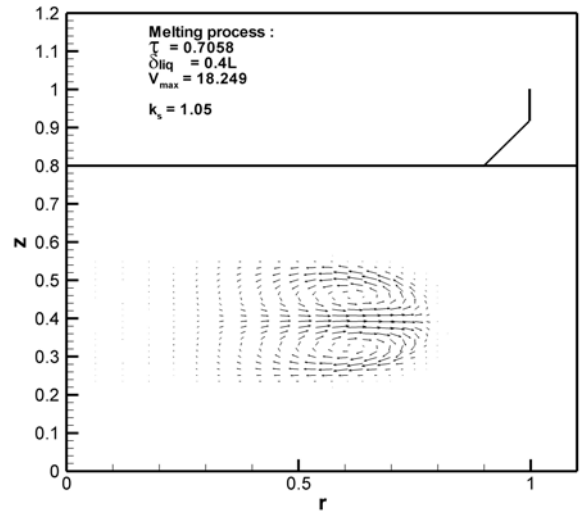
(c) $\kappa_S = 1$, $C = 1.2$

Fig. 3 Dimensionless isothermals in workpieces and electrode at time when nugget thickness δ_{liq} = 0.4L and zero for different solid-to-liquid thermal conductivity ratios and liquid-to-solid specific heat ratios.

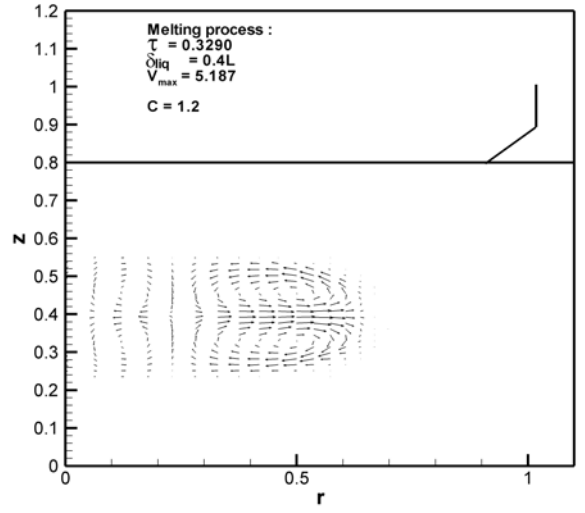
https://doi.org/10.1017/jmech.2011.3 Published online by Cambridge University Press



(a) $k_s = 1$, $C = 1.4$

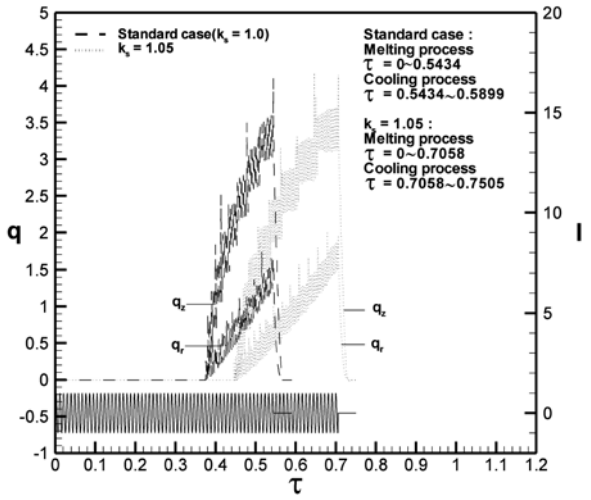


(b) $k_s = 1.05$, $C = 1.4$

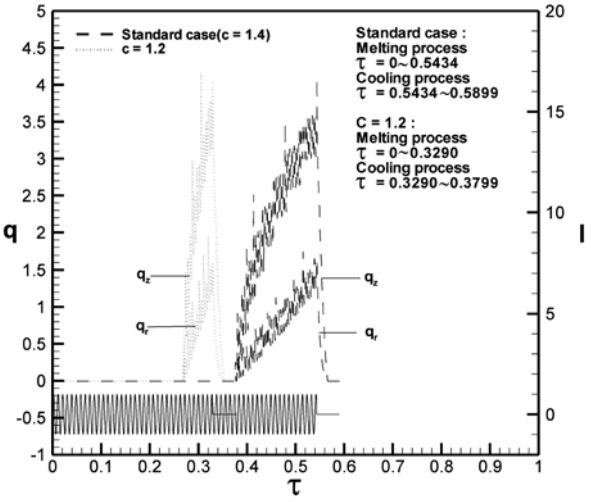


(c) $k_s = 1$, $C = 1.2$

Fig. 4 Flow patterns for different solid-to-liquid thermal conductivity ratios and liquid-to-solid specific heat ratios.



(a)



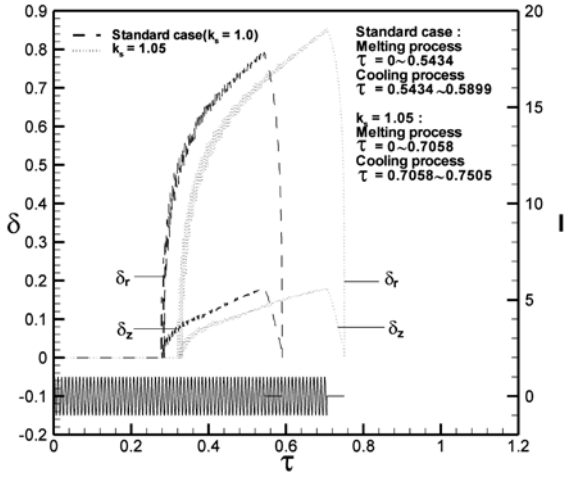
(b)

Fig. 5 Dimensionless axial and radial heat transfer rates as functions of time for different (a) solid-to-liquid thermal conductivity ratios and (b) liquid-to-solid specific heat ratios

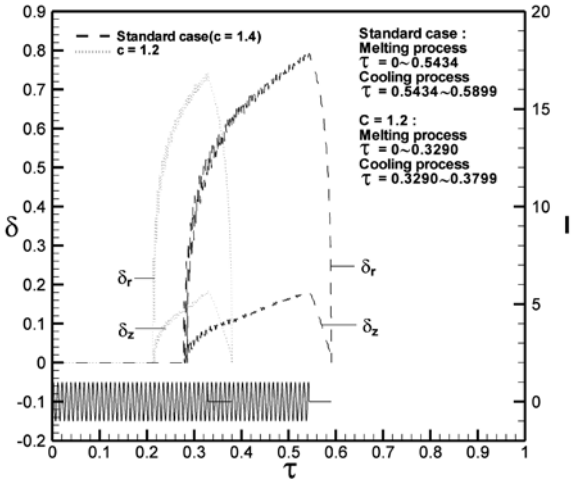
model can still lead to relevant results [14], even though it suffers 50 percent of error. Decreases in solid-to-liquid thermal conductivity ratio and liquid-to-solid specific heat ratio increase heat transfer in the axial and radial directions.

The effects of solid-to-liquid thermal conductivity ratio on dimensionless thickness and width of the molten nugget as functions of dimensionless time are shown in Fig. 6(a). In general, the growth of thickness is much less than that of width. The growth rate at the onset time is highest, whereas the molten nugget solidifies rapidly within a few cycles immediately after the moment welding current turns off. An increase in solid-liquid thermal conductivity ratio delays the nugget formation and reduces nugget growth in both the radial and axial directions. This is attributed to decreases in heat transfer in the molten nugget in both directions, as can be seen in previous figures. As liquid-to-solid specific heat ratio decreases, the onset time decreases while nugget growth increases in both the radial and axial directions, as shown in Fig. 6(b).

https://doi.org/10.1017/jmech.2011.3 Published online by Cambridge University Press



(a)



(b)

Fig. 6 Dimensionless nugget thickness and width as functions of time for different (a) solid-to- liquid thermal conductivity ratios and (b) liquid-to-solid specific heat ratios

4. CONCLUSIONS

The conclusions drawn are the following:

1. The present work realistically studies the effects of distinct thermal properties experiencing phase changes on transport variables in the course of heating, melting, cooling and freezing during resistance spot welding. Based on a realistic model of dynamic electrical resistance accounting for bulk resistance in workpieces and contact resistances at the faying surface and electrode-workpiece interfaces, AC current and magneto-hydrodynamics, the computed nugget thickness versus current agrees well with available experimental data.
2. Instead of dealing with specific materials in the literature, this work provides a general, dimensionless investigation of resistance spot welding of materials with different dimensionless properties subject to realistic working parameters.
3. Heat transfer rate in the axial direction is roughly two times higher than that in the radial direction. Decreases in solid-to-liquid thermal conductivity ratio and liquid-to-solid specific heat ratio enhance heat transfer in both the radial and axial directions.
4. In general, the growth of thickness is much less than that of width. The growth rate at the onset time is highest and gradually decreases its magnitude. The molten nugget solidifies rapidly within a few cycles after the moment welding current turns off.
5. Decreases in solid-to-liquid thermal conductivity ratio and liquid-to-solid specific heat ratio shorten time for nugget formation, and increase nugget thickness and width, and their growths.
6. Melting and solidification rates exhibit opposite results. Melting rate increases whereas solidification rate decreases by reducing solid-to-liquid thermal conductivity ratio and liquid-to-solid specific heat ratio.
7. A decrease in liquid-to-solid specific heat ratio produces two convective cells from one cell.

NOMENCLATURE

C	liquid-to-solid specific heat ratio
Da	Darcy number
f	mass fraction of liquid or solid
F_0	dimensionless parameter, as defined in Eq. (7)
f^{α}	solute mass fraction = $\tilde{f}^{\alpha} / \tilde{f}^{\alpha}_{m,0}$
$\tilde{f}^{\alpha}_{m,0}$	initial solute content
g	volume fraction or gravitational acceleration
h	enthalpy, $h = \tilde{h} / h_f$
H	magnetic field intensity in θ direction, $H = \tilde{H}\ \pi r_o / I$
H_v	hardness
h_f	fusion latent heat at eutectic point, J/kg
h_ℓ	RCT + R(1 − C) Te + 1
h_s	RT
I	welding current, amp
K	$g_s k_s + g_\ell$
k_E	thermal conductivity ratio = $\tilde{k}_E / \tilde{k}_s$
k_s	thermal conductivity ratio = $\tilde{k}_s / \tilde{k}_\ell$
K_0	permeability constant, m^2
L	distance between electrodes
L_1, L_2, L_3, L_4	length, as illustrated in Fig. 1
L_o	dimensionless parameter, as defined in Eq. (7)
M	$-(dr_c / d\zeta + \xi dN / d\zeta) / N$
N	$r_s(\zeta) - r_c(\zeta)$
n	total number of contact spots
$\mathrm{Pr_m}$	magnetic Prandtl number = $\tilde{\eta}_\ell / \tilde{\alpha}_\ell$
R	$\tilde{c}_s \tilde{T}_0 / h_f$
r_o	dimensional electrode radius, as illustrated in Fig. 1
$\tilde{R}_0$	electrical contact resistance at faying surface at T_0
s	film thickness
T	temperature = $\tilde{T} / \tilde{T}_0$
T_e	eutectic temperature

https://doi.org/10.1017/jmech.2011.3 Published online by Cambridge University Press

u, v axial and radial velocity, $u = \tilde{u}r_o / \tilde{\alpha}_\ell$, $v = \tilde{v}r_o / \tilde{\alpha}_\ell$

V velocity vector

W electrode force

Greek letters

β_s, β_T solutal and thermal expansion coefficient

δ nugget thickness

$\tilde{\eta}_\ell$ magnetic diffusivity of liquid = $1 / \tilde{\sigma}_\ell \mu_0 \mu_{r\ell}$

η_E $\tilde{\eta}_E / \tilde{\eta}_\ell$, where $\tilde{\eta}_E = 1 / \sigma_E \mu_o \mu_{rE}$

θ_o dimensionless temperature ratio, as defined in Eq. (7)

μ_r relative magnetic permeability, $\mu_r = g_\ell + g_s \mu_{rs} / \mu_{r\ell}$

ρ dimensional and dimensionless density, $\rho = \tilde{\rho} / \tilde{\rho}_\ell$

σ electrical conductivity, $\sigma = \tilde{\sigma} / \tilde{\sigma}_\ell = g_s \sigma_s + g_\ell$, mho/m

Σ dimensionless parameter, as defined in Eq. (7)

τ dimensionless time = $t\tilde{\alpha}_\ell / r_o^2$

Superscript

α solute

$\sim$ dimensional quantity

Subscript

E electrode

ℓ, liq liquid and liquidus

m mixture

s, sol solid and solidus

0 ambient

REFERENCES

1. ASM Handbook Committee, *Metals Handbook, Ninth Edition*, Volume 6 Welding, Brazing, and Soldering, ASM, OH (1983).
2. McDowell, K. H. and Weeks, D. A., "A Practical Approach to Resistance Welding," *British Welding Journal,* **6**, pp. 381–395 (1959).
3. Kou, S., *Welding Metallurgy,* Wiley, New York (1987).
4. Han, Z., Indacochea, J. E., Chen, C. H. and Bhat, S., "Weld Nugget Development and Integrity in Resistance Spot Welding of High-Strength Cold-Rolled Sheet Steels," *Welding Journal,* **72**, pp. 209s–216s (1993).
5. Xu, J., Jiang, X., Zeng, Q., Zhai, T., Leonhardt, T., Farrell, J., Umstead, W. and Effgen, M. P., "Optimization of Resistance Spot Welding on the Assembly of Refractory Alloy 50Mo-50Re Thin Sheet," *Journal of Nuclear Materials*, **366**, pp. 417–425 (2007).
6. Zhou, Y., Gorman, P., Tan, W. and Ely, K. J., "Weldability of Thin Sheet Metals during Small-Scale Resistance Spot Welding Using an Alternating-Current Power Supply," *Journal of Electronic Materials,* **29**, pp. 1090–1099 (2000).
7. Ely, K. J. and Zhou, Y., "Microresistance Spot Welding of Kovar, Steel, and Nickel," *Science and Technology of Welding and Joining,* **6**, pp. 63–72 (2001).
8. Xu, J. and Zhai, T., "The Small-Scale Resistance Spot Welding of Refractory Alloy 50Mo-50Re Thin Sheet," *Journal of Metals,* **60**, pp. 80–83 (2008).
9. Gould, J. E. and Chang, P. H., "Thermal Modeling of Spot Welds," *Journal of Metals,* **38**, pp. 39–42 (1986).
10. Wang, Y. R., Feng, J. C. and Zhang, Z. D., "Microstructure Characteristics of Resistance Spot Welds of AZ31 Mg Alloy," *Science and Technology of Welding and Joining,* **11**, pp. 555–560 (2006).
11. Wei, P. S., Huang, C. C. and Lee, K. W., "Nucleation of Bubbles on a Solidification Front-Experiment and Analysis," *Metallurgical Materials Transactions B,* **34B**, pp. 321–332 (2003).
12. Wei, P. S. and Yeh, F. B., "Factors Affecting Nugget Growth with Mushy-Zone Phase Change during Resistance Spot Welding," *Journal of Heat Transfer (Transactions ASME),* **113**, pp. 643–649 (1991).
13. Cunningham, A. and Begeman, M. L., "A Fundamental Study of Projection Welding Using High Speed Photography," *Welding Journal,* **44**, pp. 381s–384s (1965).
14. Gould, J. E., "An Examination of Nugget Development During Spot Welding, Using Both Experimental and Analytical Techniques," *Welding Journal,* **66**, pp. 1s–10s (1987).
15. Wei, P. S. and Ho, C. Y., "Axisymmetric Nugget Growth During Resistance Spot Welding," *Journal of Heat Transfer (Transactions ASME)*, **112**, pp. 309–316 (1990).
16. Feng, J. C., Wang, Y. R. and Zhang, Z. D., "Nugget Growth Characteristic for AZ31B Magnesium Alloy during Resistance Spot Welding," *Science and Technology of Welding and Joining,* **11**, pp. 154–162 (2006).
17. Podržaj , P., Polajnar, I., Diaci, J. and Karižˇ , Z., "Influence of Welding Current Shape on Expulsion and Weld Strength of Resistance Spot Welds," *Science and Technology of Welding and Joining,* **11**, pp. 250–254 (2006).
18. Roberts, W. L., "Resistance Variations During Spot Welding," *Welding Journal,* 30, pp. 1004–1019 (1951).
19. Greenwood, J. A., "Temperatures in Spot Welding," *British Welding Journal,* **8**, pp. 316–322 (1961).
20. Wei, P. S., Wang, S. C. and Lin, M. S., "Transport Phenomena During Resistance Spot Welding," *Journal of Heat Transfer (Transactions ASME),* **118**, pp. 762–773 (1996).
21. Li, Y. B., Lin, Z. Q., Hu, S. J. and Chen, G. L., "Numerical Analysis of Magnetic Fluid Dynamics Behaviors during Resistance Spot Welding," *Journal of Applied Physics,* **101**, pp. 1–10 (2007).
22. Wang, S. C. and Wei, P. S., "Modeling Dynamic Electrical Resistance during Resistance Spot Welding," *Journal of Heat Transfer (Transactions ASME)*, **123**, pp. 576–585 (2001).
23. Bennon, W. D. and Incropera, F. P., "A Continuum Model for Momentum, Heat and Species Transport in Binary Solid-Liquid Phase Change Systems - I. Model Formulation," *International Journal for Heat and Mass Transfer,* **30**, pp. 2161–2170 (1987).
24. Patankar, S. V., *Numerical Heat Transfer and Fluid Flow*, Hemisphere, New York (1980).

(Manuscript received April 12, 2010,
accepted for publication July 12, 2010.)

https://doi.org/10.1017/jmech.2011.3 Published online by Cambridge University Press